

# Physical interpretation of a pulsed atmospheric pressure plasma jet following parametric study of the UV-to-NIR emission

Cite as: Phys. Plasmas **27**, 123503 (2020); <https://doi.org/10.1063/5.0031065>

Submitted: 28 September 2020 . Accepted: 08 November 2020 . Published Online: 10 December 2020

 K. Gazeli,  P. Svarnas,  C. Lazarou,  C. Anastassiou,  G. E. Georghiou,  P. K. Papadopoulos, and F. Clément



View Online



Export Citation



CrossMark

## ARTICLES YOU MAY BE INTERESTED IN

[Electric field dynamics in an atmospheric pressure helium plasma jet impinging on a substrate](#)  
Phys. Plasmas **27**, 123505 (2020); <https://doi.org/10.1063/5.0021837>

[Electrodeless atmospheric secondary induced ionization jet \(EASII-jet\): Dynamics and properties of a transferred helium plasma source](#)  
Phys. Plasmas **27**, 123504 (2020); <https://doi.org/10.1063/5.0027640>

[Discharge properties of a coaxial plasma jet at different microwave frequencies](#)  
Phys. Plasmas **27**, 123508 (2020); <https://doi.org/10.1063/5.0020243>

Physics of Plasmas

**SPECIAL TOPIC:** Plasma Physics  
from the Magnetospheric Multiscale Mission

Submit Today!



# Physical interpretation of a pulsed atmospheric pressure plasma jet following parametric study of the UV-to-NIR emission

Cite as: Phys. Plasmas **27**, 123503 (2020); doi: [10.1063/5.0031065](https://doi.org/10.1063/5.0031065)  
Submitted: 28 September 2020 · Accepted: 8 November 2020 ·  
Published Online: 10 December 2020









View Online



Export Citation



CrossMark

K. Gazeli,<sup>1,2,a),b)</sup>  P. Svarnas,<sup>1</sup>  C. Lazarou,<sup>3,4</sup>  C. Anastassiou,<sup>4</sup>  G. E. Georghiou,<sup>3,4</sup>  P. K. Papadopoulos,<sup>5</sup>   
and F. Clément<sup>2</sup>

## AFFILIATIONS

<sup>1</sup>High Voltage Laboratory, Electrical and Computer Engineering Department, University of Patras, 26 504 Rion-Patras, Greece

<sup>2</sup>Institute of Analytical Sciences and Physico-Chemistry for Environment and Materials (IPREM), UPPA, CNRS UMR 5254, 2 Avenue Président Angot, 64 000 Pau, France

<sup>3</sup>FOSS Research Centre for Sustainable Energy, Department of Electrical and Computer Engineering, University of Cyprus, Nicosia 1678, Cyprus

<sup>4</sup>Electromagnetics and Novel Applications Laboratory (ENAL), Department of Electrical and Computer Engineering, University of Cyprus, Nicosia 1678, Cyprus

<sup>5</sup>Department of Mechanical Engineering and Aeronautics, University of Patras, 26 504 Rion-Patras, Greece

<sup>a)</sup>Author to whom correspondence should be addressed: [kristaq.gazeli@gmail.com](mailto:kristaq.gazeli@gmail.com)

<sup>b)</sup>Present address: University Sorbonne Paris Nord, LSPM, CNRS, UPR 3407, F-93430 Villetaneuse, France.

## ABSTRACT

In the present report, an atmospheric pressure plasma jet is sustained in a helium channel by high square wave unipolar voltage. The gas flow rate and the square wave features (amplitude, frequency, and duty cycle) are varied over a wide range, while the plasma ultraviolet to near infrared emission is recorded. The plasma emission pattern, the propagation dynamics of the involved ionization fronts, the relative density of critical excited species, and the rotational and vibrational temperatures of neutral and ionic species are measured. An optimum operational window is found corresponding to a helium flow rate of 2 slm, a pulse amplitude of 7.5 kV, a pulse repetition rate of 10 kHz, and a pulse duty cycle of 5%–7%. Under these conditions, a plasma jet length close to 45 mm and a gas temperature close to 325 K are obtained, while a high yield of OH, N<sub>2</sub>(SPS), N<sub>2</sub><sup>+</sup>(FNS), N<sub>2</sub>(FPS), He\*, O\*, and NOγ is achieved. The results are found to be in good agreement with the bibliography and motivate a consideration on the involved physical mechanisms. The plasma jet propagation with respect to the reactive species production is discussed based on the local electric field variation over the high voltage pulse width.

Published under license by AIP Publishing. <https://doi.org/10.1063/5.0031065>

## I. INTRODUCTION

Atmospheric pressure cold plasmas for various technological applications are conventionally based on dielectric-barrier discharges (DBDs) developed between different electrode configurations.<sup>1–5</sup> Depending on the electrodes, the barrier relative configuration, the working gas, and the driving electric field, plasmas of variable patterns and physicochemical properties can be produced for targeted applications.<sup>1,3–6</sup> The dominant position among the potential schemes is held by the widely studied plasma jets of noble gases. It is well established that in this case, ionizing fronts having ultrasonic velocities are generated<sup>2,7,8</sup> and propagate under a complicated interplay. This interplay involves the local reduced electric field, the plasma species and

radiation from vacuum ultraviolet (VUV) up to near-infrared (NIR),<sup>9,10</sup> the dielectric surfaces, and the hydrodynamic fields of both the noble and the surrounding air gases.<sup>11–13</sup>

Plasmas in the above DBD-based systems are commonly sustained by either continuous sinusoidal or pulsed unipolar high voltages. In the latter case, arbitrary waveforms or well-defined square waves are employed. Arbitrary waveforms can lead to the appearance of damped oscillations, surges and variations on the front or/and the tail of the discharge, an even undefined ratio of the pulse width to the pulse period (duty cycle), etc.<sup>14–16</sup> Despite the potential deficiency of these driving waveforms and the difficulty of suppressing those “imperfections” when the pulses lie on the ns scale, arbitrary

waveforms are used for various applications (e.g., sterilization) due to their low cost and ease of production. However, due to the capacitive behavior of the DBD-based reactors, any variation of the driving voltage directly affects the discharge current, which, in turn, mirrors the ionization processes. On the other hand, well-defined high voltage square pulses have efficiently been used for fundamental studies and determination of controllable and reproducible operational windows. Demonstrative examples are the subtle interpretation of electrohydrodynamic effects,<sup>17</sup> the investigation of the propagation of reactive species,<sup>18</sup> plasma jet current and DBD power measurements with high accuracy,<sup>19</sup> and the manipulation of the propagation dynamics of fast-moving ionization fronts.<sup>20</sup>

Accordingly, the present work is devoted to the study of a DBD-based helium plasma jet driven by high voltage square pulses. The pulse amplitude, frequency, and duty cycle, along with the gas flow rate, are varied over intervals commonly adopted by different research groups, and their role in the plasma reactivity is experimentally determined. Namely, ultraviolet to near infrared (UV-to-NIR) emission measurements are carried out, providing information on the plasma emission pattern, the ionization front velocity, the rotational and vibrational temperatures of neutral and ionic species, and the relative density of critical excited species. Optimum working conditions are unveiled, while the present communication provides concluding data for the parameterization of similar plasma setups. The results are finally discussed with respect to published reports. Evidence is provided on the importance of the duty cycle in the plasma jet physical and chemical properties. The latter is interpreted from different points of view.

## II. EXPERIMENTAL SETUP

The layout of the DBD configuration employed for the plasma jet production is provided in Fig. 1(a). It mainly consists of a quartz capillary tube (1.14 mm inner and 2.5 mm outer diameter), a thin tungsten wire (0.125 mm diameter), and a brass hollow cylinder (10 mm outer diameter and 10 mm length). The wire is housed in the tube, keeping a distance of 20 mm between its tip and the tube orifice, and it is electrically driven. The hollow cylinder is tightly fixed on the outer surface of the tube, being aligned with the tip of the wire, and it is grounded. In this way, a coaxial electrode configuration is formed. The working gas is high-purity helium (He; Linde plc; 99.999%). The gas flow is downward, and it is adjusted between 0.2 and 2 standard liters per minute (slm) through a mass flow controller (MFC; Bronkhorst® High-Tech EL-FLOW). Thus, an open space plasma jet is developed perpendicular to the radial DBD, which is confined by the coaxial electrode configuration [Fig. 1(b)].<sup>21</sup>

The plasma is sustained by a custom-made power supply, which generates positive square pulses of adjustable amplitude (0 to 20 kV), frequency (up to 100 kHz), pulse width (0.5 to 80  $\mu$ s), and rise time (100 ns). Here, the operating parameters are varied as follows: voltage, 3.5–7.5 kV; frequency, 1–15 kHz; and duty cycle, 0.5%–60%. The voltage and the DBD total current (i.e., drift + displacement) are recorded simultaneously on a digital oscilloscope (Tektronix® TDS3054B; 500 MHz; 5 GSamples  $s^{-1}$ ). A wideband high voltage divider (Tektronix® P6015A; DC to 75 MHz) and a current transformer (Pearson Electronics® 6585; 400 Hz–200 MHz; 0.5 V  $A^{-1}$  at 50  $\Omega$ ) are used. The above waveforms are continuously monitored to ensure stable operation of the plasma jet. Additionally, the discharge

operates for 30 min before the execution of any experiment. This time interval is selected according to previous studies,<sup>22</sup> ensuring thermal stabilization of the system and, eventually, reproducible results.

To qualitatively study the evolution of the plasma emission pattern under different operating conditions, a high-definition, digital single-lens reflex (DSLR) camera (Nikon® D3100) is used. Additionally, the use of an axially movable optical fiber (Ceramopectec® UV 1500/1590N; OF 2 in Fig. 1) along with a photo-electron multiplier tube (Hamamatsu R928; 185–900 nm; PMT 2 in Fig. 1) allows for the precise measurements of the length of the plasma jet (here, “length” refers to the “extension” of the plasma outside the tube). The fiber is coupled with an optical diaphragm to collect light from a specific solid angle corresponding to a well-defined axial zone of 5 mm. Thus, during the fiber translation, spatial overlapping is carefully avoided.

To investigate the propagation dynamics of the ionization fronts, an additional PMT is used (PMT 1 in Fig. 1; identical to PMT 2), which is coupled with an additional optical fiber (OF 1 in Fig. 1; identical to OF 2). Both fibers are connected to identical optical diaphragms, which limit the probed zone to 5 mm axially and are set at fixed axial positions. Thus, the center of OF 1 is fixed at a distance of  $d_1 = 2.5$  mm from the reactor’s tube orifice and that of the OF 2 at  $d_2 = 12.5$  mm. Based on this setup, PMT 1 detects the emission induced during the propagation of a single ionization front before PMT 2. Hence, the average propagation velocity is approximated as the quotient of the fixed distance between the probed zones ( $d_2 - d_1$ ) divided by the time lag between the two PMT signals.

The analysis of the wavelength-resolved plasma jet emission in the UV-to-NIR range is achieved by means of optical emission spectroscopy. The emitted light is collected using OF 2, which is now connected to a high-resolution spectrometer (1000M Jobin Yvon®; 1200 grooves  $mm^{-1}$  grating; blazed at 500 nm) coupled with a charge-coupled device (Spectrum ONE CCD-3000V; CCD). The spectrometer is calibrated in terms of wavelength units using an appropriate spectral lamp (Oriel® 6035 Hg–Ar). Besides, attention is paid for the calibration of the entire spectroscopic system (optical fiber, spectrometer, and detector) in terms of relative spectral efficiency. This is realized by using a standard calibration lamp (Newport® 6333) operating at a temperature of 3300 K. By considering the theoretical spectral irradiance of a black body at this temperature and the experimental spectrum of the lamp in the wavelength range of 300–900 nm, adequate calibration factors are derived and used for the correction of the experimental spectra. In the spectral range of 200–300 nm, the irradiance of the lamp is very weak to allow for a reliable calibration. Therefore, the relative intensity of the spectra recorded in the above two ranges cannot be directly compared.

High-resolution spectroscopic data are further exploited for evaluating the gas temperature. The rotational temperature of three probe molecules, which are dominant in the emission spectrum, are used. Namely, OH ( $A, v' = 0 - X, v'' = 0$ ) at 306.4 nm,  $N_2$ (SPS) ( $C, v' = 0 - B, v'' = 0$ ) at 337.1 nm, and  $N_2^+$ (FNS) ( $B, v' = 0 - X, v'' = 0$ ) at 391.4 nm. The rotational temperature is evaluated by fitting the experimentally obtained rotational spectra with synthetic spectra generated by a lab-made code.<sup>23,24</sup> The accuracy of the entire process is estimated to be around  $\pm 40$  K. The estimation of the gas temperature from the rotational temperature of excited states of probe molecules (in the present case  $A^2\Sigma^+$ ,  $C^3\Pi_u$ , and  $B^2\Sigma^+$  corresponding to OH,  $N_2$ , and  $N_2^+$ ,

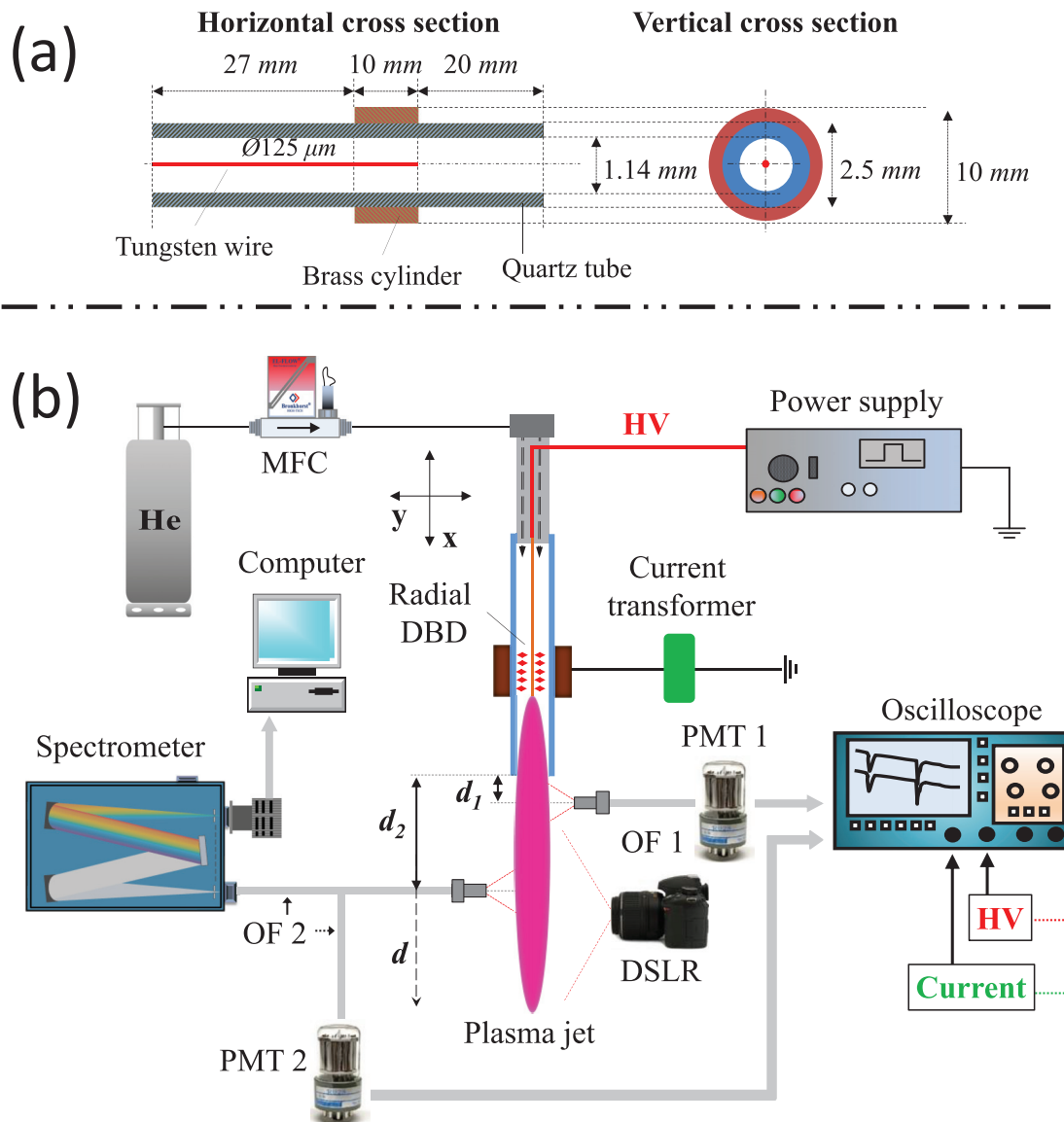


**FIG. 1.** Conceptual view of the experimental setup. (a) Details of the DBD design. (b) DBD reactor, power and gas supply, and installed diagnostics. MFC, DSLR, OF, and PMT stand for the mass flow controller, digital single-lens reflex, optical fiber, and photo-electron multiplier tube, respectively.

respectively) is valid if they are in thermodynamic equilibrium with the surrounding gas molecules. This condition is fulfilled if the characteristic time of the rotational–translational relaxation is shorter than the radiative lifetime of these states and the collision frequency is sufficiently high.<sup>25,26</sup> Then, the rotational population of the excited states is thermalized before the emission occurs and the gas temperature can be inferred by the rotational temperature. For most of the atmospheric pressure plasma jet systems operating in helium, the latter statement is particularly true for the OH and the N<sub>2</sub>(SPS) molecules.<sup>25,26</sup>

On the other hand, the evaluation of the vibrational temperature of probe-excited molecules is often useful to verify the non-equilibrium behavior of the plasma.<sup>27</sup> The vibrational excitation

indicates the efficiency of the energy exchange between free electrons and molecules. Indeed, several molecules, such as N<sub>2</sub> and O<sub>2</sub>, are available in the ambient air surrounding the plasma jet and are vibrationally excited through electron impacts. These species can accumulate fairly large amounts of energy, which can be used in chemical reactions.<sup>28</sup> Herein, the vibrational temperature is evaluated via the Boltzmann-plot method, which has been proven to be an effective technique for this purpose.<sup>29,30</sup> The first three band heads of the vibrational sequence  $\Delta v = -2$  of the N<sub>2</sub>(SPS) molecule are considered. The fingerprint of this transition is found in the wavelength range of 365–385 nm. The evaluation method is explained in detail elsewhere.<sup>31</sup> The estimated error is around  $\pm 6\%$ , mainly resulting from the air



temperature and humidity changes between different series of experiments and the linear regression errors during data processing.

If not mentioned otherwise, the default working conditions are 7.5 kV, 2 slm, 10 kHz, and 1%, and the probed zone of optical emission is along 5 mm downstream of the reactor's tube orifice. When applicable, mean values and error bars are obtained from two independent series of experiments.

### III. RESULTS

Figure 2 shows representative oscillograms of the high voltage driving pulse and the induced total DBD current. The current waveform consists of impulses following the rising and falling edges of the voltage pulse. These impulses result from the capacitive and drift current components of the radial DBD.<sup>7,19,21</sup> In parallel, ionization fronts propagate axially, following the helium flow direction.<sup>2,7,21</sup> This propagation is reflected on the plasma emission recorded downstream of the tube orifice, and it is clearly correlated with two discrete ionization fronts (blue curve in Fig. 2; the negative values are due to the PMT negative bias). The nature of such fronts has been studied extensively,<sup>32</sup> whereas the present work aims to conduct a parametric study of major UV-to-NIR features of the plasma jet induced by those fronts.

Figure 3 manifests the dependence of the plasma jet visible pattern on the working parameters. Two different types of data are given, and a fair agreement is achieved between them. The first set of data (solid symbols) refers to the plasma jet length evaluated with PMT 2, and the second set (inset photos) refers to digital images of the visible plasma jet downstream of the tube orifice (a part of the quartz tube is also shown for clarification reasons).

Any increase in the voltage amplitude or helium flow rate continuously induces a longer plasma jet, while the plasma channel appears laminar. On the contrary, the increase in the voltage duty cycle hinders the plasma jet expansion. Even more, the frequency influence on the plasma jet length is not monotonous, and it alters the gas flow field too. In Fig. 3(c), a transition to turbulences is observed when the system is driven at 1 and 3 kHz.

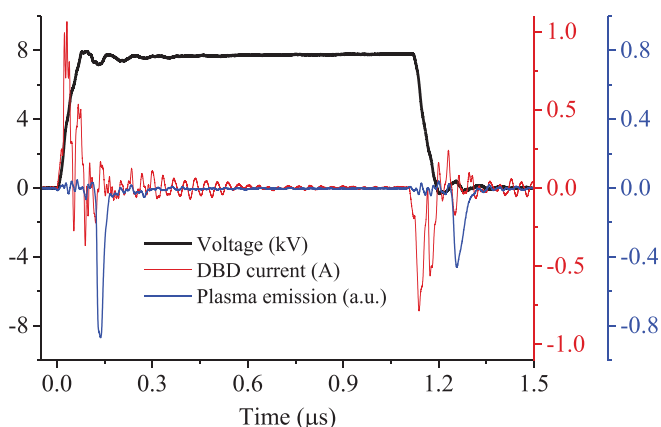


**FIG. 2.** Typical oscillograms of the driving pulsed voltage, the induced total DBD current, and the ionization front emission. The emission is wavelength integrated over the UV-to-NIR range, and the probed zone is along 5 mm downstream of the reactor's tube orifice. Working conditions: 7.5 kV, 0.2 slm, 10 kHz, and 1%.

Figure 4 presents the mean velocity of the ionization fronts developed during the rising and falling edges of the driving pulse (see Fig. 2), for the corresponding parameters of Fig. 3. Velocities up to about  $3.5 \times 10^7$  cm s<sup>-1</sup> are measured. Independent of the conditions, the ionization front, which is developed during the rising part of the driving voltage, propagates faster, and the velocity of both fronts increases with the voltage amplitude and the helium flow rate. In contrast, similar to the results of Fig. 3, the voltage frequency and duty cycle affect differently the plasma jet operation. The frequency does not significantly affect the propagation of the ionization front related to the positive slope of the voltage, and, still more, the increase in the duty cycle percentage slows down the propagation of the front related to the negative slope of the voltage. The above-mentioned observations are discussed in detail in Sec. IV.

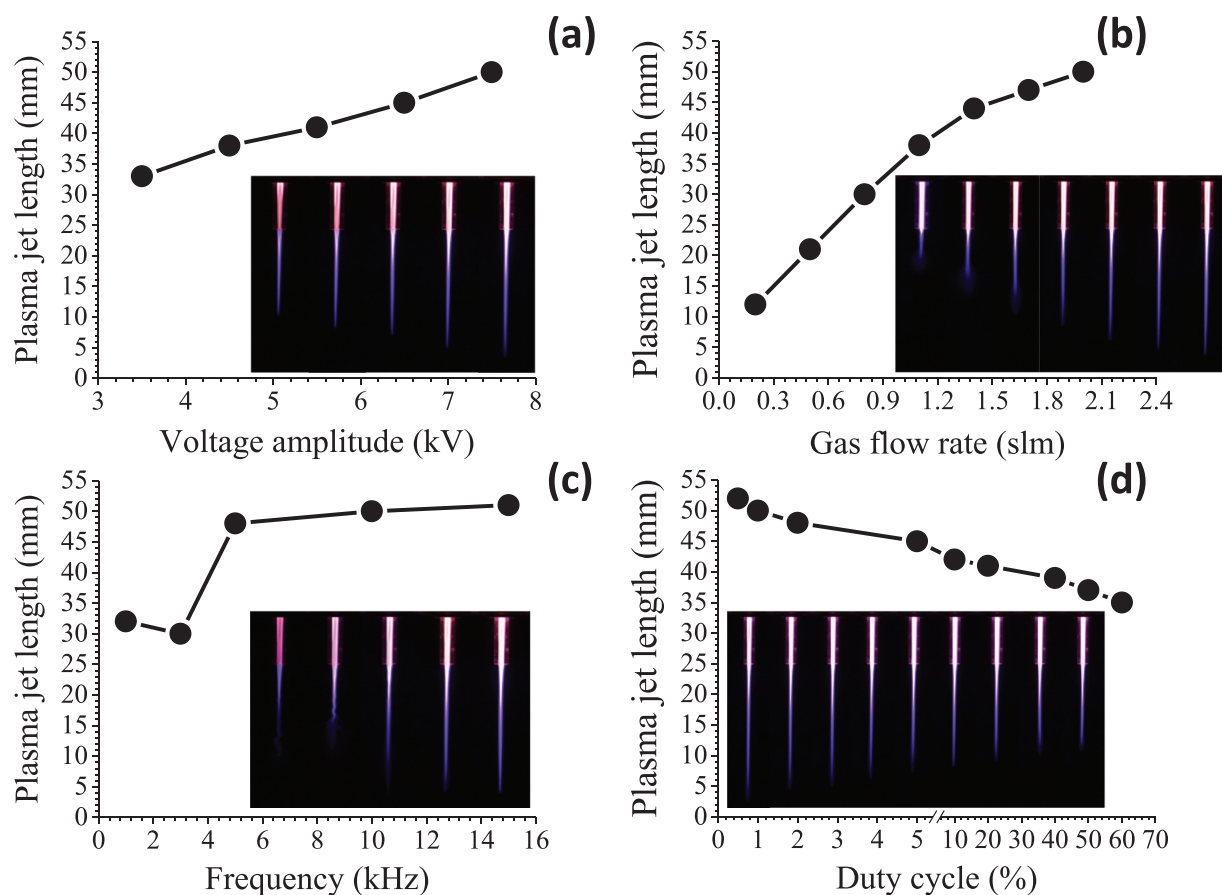
Deeper insight into the role of the working parameters can be gained by identifying the main excited emissive species induced by the ionization front's propagation. Figure 5 shows the UV-to-NIR optical emission wide-scan spectrum of the plasma jet under the default working conditions and identifies the emissive reactive species that are produced. Several reactive oxygen and nitrogen species (RONS) are found, with the corresponding wavelengths and transitions tabulated in Ref. 31. The systematic study of this spectrum vs the working parameters of the plasma jet leads to the results in Figs. 6–8.

Figure 6 shows the dependence on the working parameters of the relative density of main excited neutral and ionic species produced by the present plasma jet.

A higher voltage amplitude promotes an enhanced species production [Fig. 6(a)] probably due to the higher reduced electric field, which, in turn, leads to more efficient electron–neutral collisions. The corresponding curves are convex. Similarly, as the helium flow rate increases, the helium channel is better established in air and the generated plasma jet becomes enriched with reactive emissive species [Fig. 6(b)]. The corresponding curves are now concave. The above remarks are reflected on the brighter branch of the jet close to the reactor orifice [Figs. 3(a) and 3(b)]. One notable exception from Fig. 6(b) is that a flow rate higher than 1 slm does not significantly affect the excited nitrogen density close to the reactor orifice.

Keeping the duty cycle constant (1%), the frequency increment results in the species density increase [Fig. 6(c)]. The intensity of the molecular nitrogen does not further increase for frequencies higher than 10 kHz. It should be noted that the frequency is directly related to the power supplied to the system.<sup>22</sup> The power increase leads to higher energy deposited onto physicochemical reactions. On the other hand, by keeping the frequency constant (10 kHz), the predominant role of the duty cycle in the chemical reactivity of a pulsed plasma jet can be seen in Fig. 6(d). An optimum value of about 5% of duty cycle achieves enhanced densities apart from that of molecular nitrogen, which is maximum at 7%. Both the frequency and the duty cycle play a crucial role in the plasma chemistry through different interconnected paths, which are discussed extensively in Sec. IV.

Figures 7 and 8 focus on the two extreme bands of the optical emission spectrum, i.e., UV-C and IR-A. These two regions are associated with nitric oxide (specifically NO $\gamma$ ) and the first positive system of nitrogen [N<sub>2</sub>(FPS)], which are significant agents in plasma chemistry and biological applications.<sup>33,34</sup> Their parametric study is a goal of the present work, and the results show that (i) as the voltage amplitude increases up to 7.5 kV, the densities of both species increase



**FIG. 3.** Measured length from captured images (ISO: 100,  $f/5.6$ , 2 s) of the plasma jet pattern vs (a) voltage amplitude, (b) helium flow rate, (c) voltage frequency, and (d) voltage duty cycle.

significantly; (ii) as the helium flow rate increases up to about 1–1.4 slm, the densities of both species approach a maximum value, showing either a slight decay [Fig. 7(b)] or a quasi-saturation [Fig. 8(b)] thereafter; (iii) as the voltage frequency increases up to 15 kHz, the densities of both species increase significantly; and (iv) as the voltage duty cycle increases up to 5%, the densities of both species increase, showing a slight decay thereafter.

Another critical property of the plasma jets with respect to various applications is the gas temperature, which is studied parametrically as explained in Sec. II. Figures 9(a)–9(c) depict the method followed for the rotational temperature evaluation, i.e., the fitting of numerically developed rotational distributions to the experimentally determined ones. Three different probe species are considered: OH(A),  $N_2(C)$ , and  $N_2^+(B)$ . Figure 9(d) depicts the method followed for the vibrational temperature evaluation, i.e., Boltzmann plots. The first three band heads of the vibrational sequence  $\Delta v = -2$  of the  $N_2(SPS)$  molecule are considered.

The evolution of both temperatures (rotational and vibrational) as a function of the working parameters is presented in Figs. 10 and 11, respectively. As a general comment, the rotational and vibrational temperatures do not change significantly when the voltage amplitude, helium flow rate, voltage frequency, and voltage duty cycle are varied.

However, there are some worth mentioning remarks: (i) the gas temperature, expressed by the rotational temperature of the three excited species, is around 300–325 K, i.e., fairly low. (ii) the higher temperature (around 325–375 K) resulting from the  $N_2^+(FNS)$  molecular ion should be attributed to the generation of helium metastables and helium dimer ions in the plasma jet. These molecules contribute effectively to the ionization–excitation of  $N_2(X)$  at the  $N_2^+(B)$  level due to the well-known Penning ionization mechanism. In this case,  $N_2^+(B)$  is expected to be excited at high rotational energy levels along with an overpopulation of this excited state. There is, thus, the absence of equilibrium between these molecular ion rotational degrees of freedom and the translational ones of the gaseous species (i.e., gas temperature), leading to higher rotational temperatures.<sup>25,34</sup> Such mechanisms do not occur for the other two probe molecules under the present experimental conditions, and their rotational temperature remains close to the room one. (iii) The increase in the gas flow rate tends to lower the gas temperature [Fig. 10(b)] as it has been recorded previously in similar systems.<sup>22</sup> This fact is better expressed by the OH(A) than the  $N_2(C)$  molecule. OH(A) has been accepted as a more reliable molecule for rotational temperature measurements.<sup>35,36</sup> (iv) the vibrational temperature is about one order of magnitude higher than the rotational temperature, confirming the production of a plasma being out of

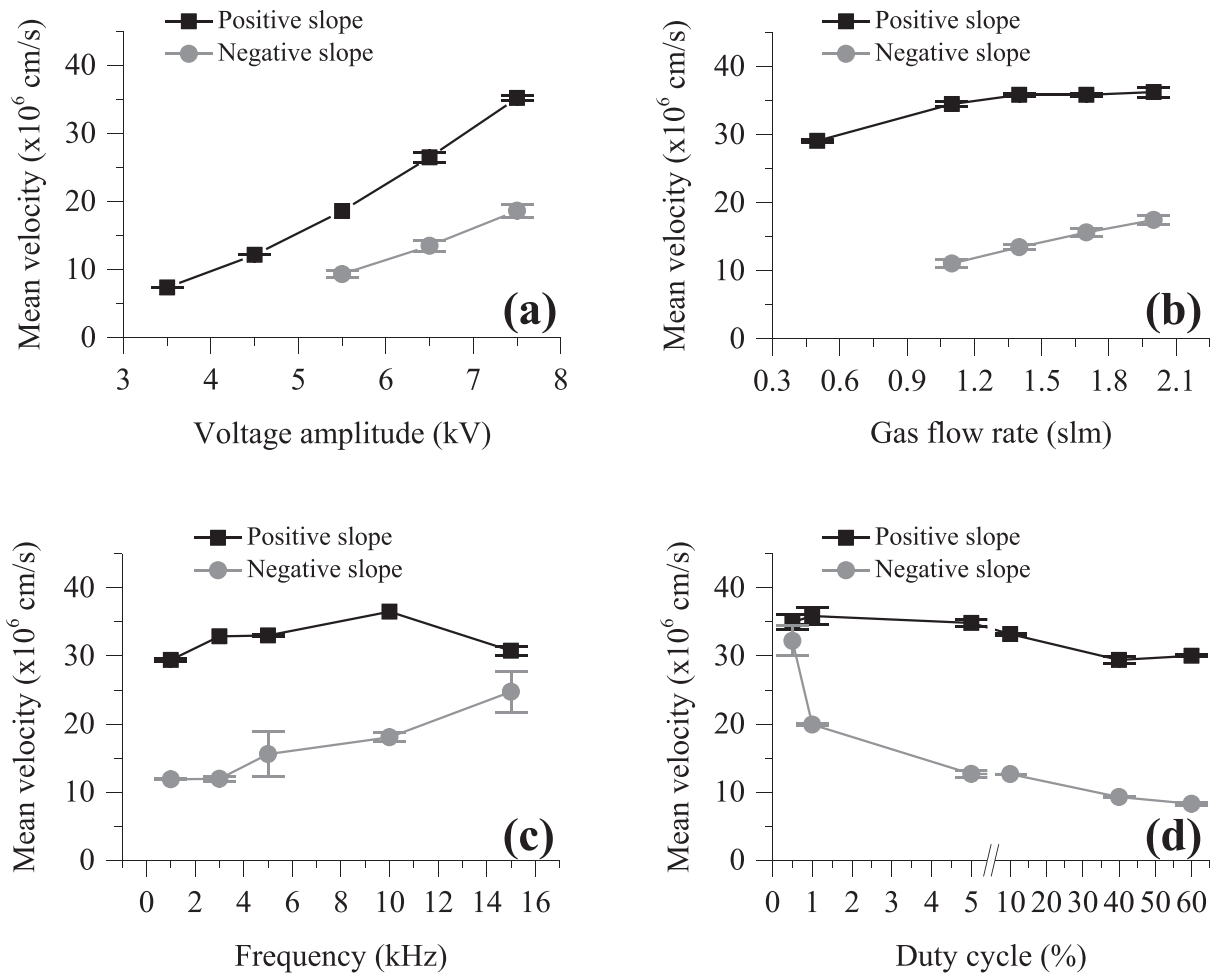


**FIG. 4.** Mean propagation velocity of the two ionization fronts generated during the positive and negative slopes of the driving voltage, respectively, vs: (a) voltage amplitude, (b) helium flow rate, (c) voltage frequency, and (d) voltage duty cycle.

thermodynamic equilibrium. Values between about 3250 and 3500 K are obtained independent of the working conditions.

**IV. DISCUSSION**

The plasma under investigation emerges from a helium jet being channeled in open space and being ionized due to the application of high voltage square pulses of positive polarity to a DBD-based reactor. Two ionization fronts are formed (see PMT signals in Fig. 2 and velocity values in Fig. 4), one during the positive slope of the voltage pulse and a second one, being weaker and slower, during the negative slope.

The first front resembles to a cathode-directed streamer although, strictly speaking, it should be distinguished from that in some respects.<sup>32</sup> Briefly, when the voltage pulse rises up to its plateau and is sustained there (pulse width phase), primary electrons are accelerated and electronic avalanches propagate toward the biased electrode, ionizing and exciting atoms and molecules along their path. The resultant positive ions propagate much slower toward the opposite direction. The typical mean time needed for the cathode-directed streamer development and propagation along the observed plasma jet is around

$5 \text{ cm}/(3 \times 10^7 \text{ cm s}^{-1}) \approx 0.17 \mu\text{s}$  (Figs. 3 and 4). Although this value may be misjudged since the instantaneous velocity varies considerably over propagation,<sup>2,8,18,37</sup> the minimum pulse width used here is about  $0.67 \mu\text{s}$  (1% at 15 kHz), which is adequate for the streamer formation and propagation.<sup>18,32,36,37</sup>

Once the streamer vanishes, the post-streamer phase begins, and a residual positive ionic charge is found downstream of the tube orifice.<sup>11,17</sup> Throughout the post-streamer phase only long-lived excited states<sup>51</sup> and residual ionic charge formed in the wake of the cathode-directed streamer propagation exist. The local field weakens since the space charge field opposes the externally applied electric field. For longer pulse widths, the externally applied field exerts prolonged force to the residual ionic charges, forcing it to drift apart.

When the voltage pulse falls to zero after a certain time, which is defined by the pulse width, the externally applied electric field returns to zero and the local electric field is now determined by the residual ionic charges only. Under the influence of this field, primary electrons are accelerated downstream of the tube orifice and a second ionization front is now developed and propagates (see the PMT signal over the

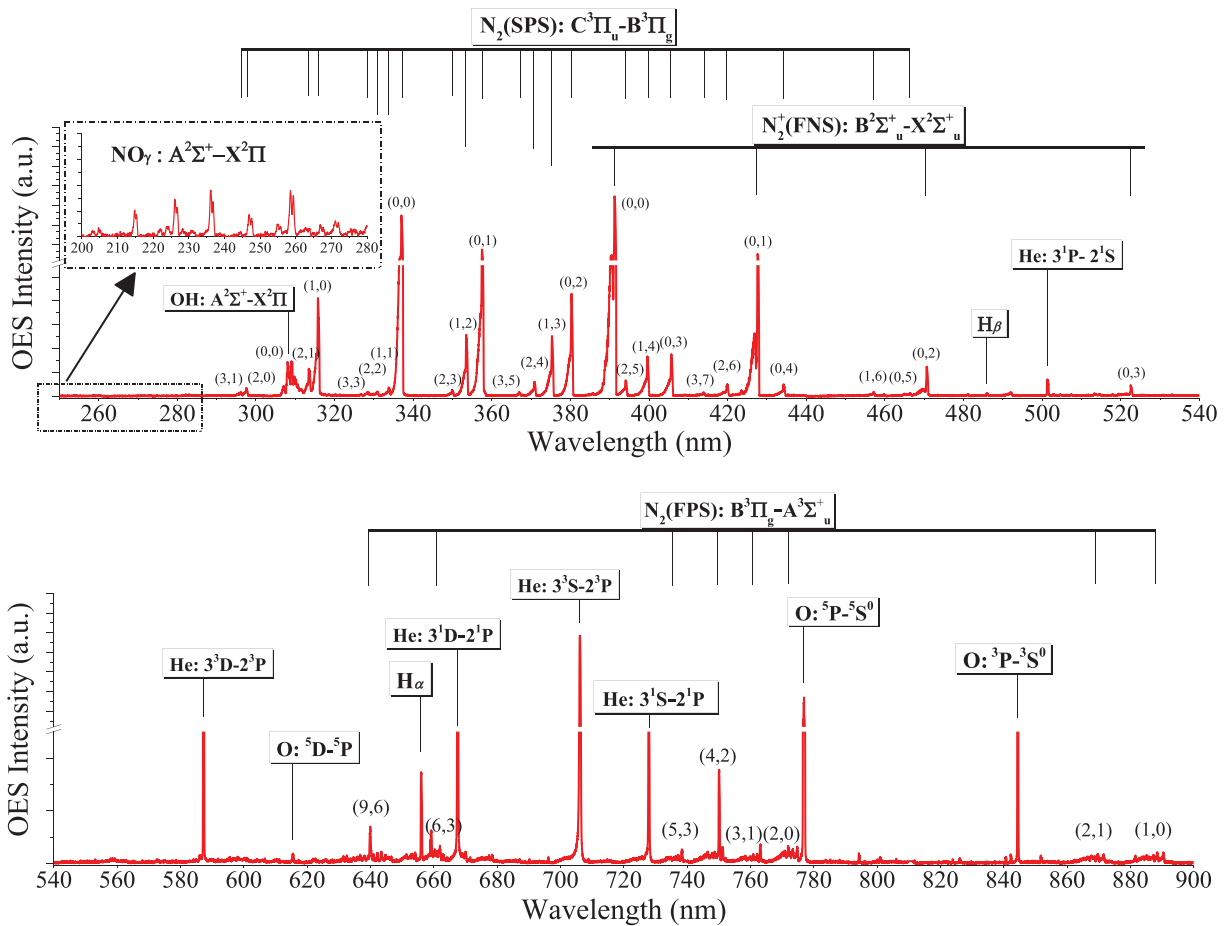


**FIG. 5.** UV-to-NIR wide-scan spectrum emitted by the plasma jet. The spectrum is spatially integrated over the entire plasma jet length (about 50 mm), and it is calibrated in terms of wavelength units and relative intensity.

negative slope in Fig. 2). For a similar electrode-barrier configuration and driving voltage, it has been mentioned that this weak second discharge ignites because of the voltage induced by the charges, which have accumulated on the surface of the dielectric tube during the previous discharge.<sup>37</sup> However, this scenario is debatable because the positively driven electrode is not covered by dielectric, and thus, charge could accumulate on the inner surface of the dielectric tube only. This charge should be positive, and this cannot explain the direction of the electron drift during the second front propagation.

For long enough pulse widths, the second ionization front is subjected to a weaker local electric field at the instant of its ignition since the residual charge has previously drifted apart. Therefore, the second ionization front appears weaker and slower. This could explain the important decrease in mean velocity in Fig. 4(d) (negative slope), the slight decrease in the plasma jet in Fig. 3(d), and the slight decrease in the chemical reactivity in Figs. 6(d), 7(d), and 8(d) for long enough duty cycles. It is reminded that the cathode-directed streamer is the one that determines principally the properties of a positively driven plasma jet,<sup>7,17</sup> and it is not affected much by the pulse width; it is principally related to the

characteristics of the rising part of the high voltage pulse. This is reflected by the small variation of its mean velocity vs the duty cycle, compared to that of the second front [Fig. 4(d)].

Variation of the pulse width can take place either by keeping the pulse frequency constant and adjusting the duty cycle or by keeping the duty cycle constant and adjusting the frequency. In Figs. 3(c), 4(c), 6(c), 7(c), and 8(c) the duty cycle is fixed at 1%, and the frequency varies from 1 to 15 kHz, resulting in pulse widths from 100 to 6.7  $\mu$ s, respectively. As the frequency is increasing (i.e., the pulse width is decreasing), the cathode-directed streamer velocity remains almost constant [Fig. 4(c); positive slope], the second front velocity increases significantly [Fig. 4(c); negative slope], the plasma jet length increases [Fig. 3(c)], and the chemical reactivity is enhanced [Figs. 6(c), 7(c), and 8(c)]. Although these tendencies agree with the above-mentioned concept of the role of the residual ionic space charge in the second front propagation, the important increase in the plasma jet length and the enhancement of the chemical reactivity (which depend mostly on the cathode-directed streamer as mentioned above) should be mainly attributed to the higher power injected into the system (power is almost proportional to the frequency<sup>22</sup>).

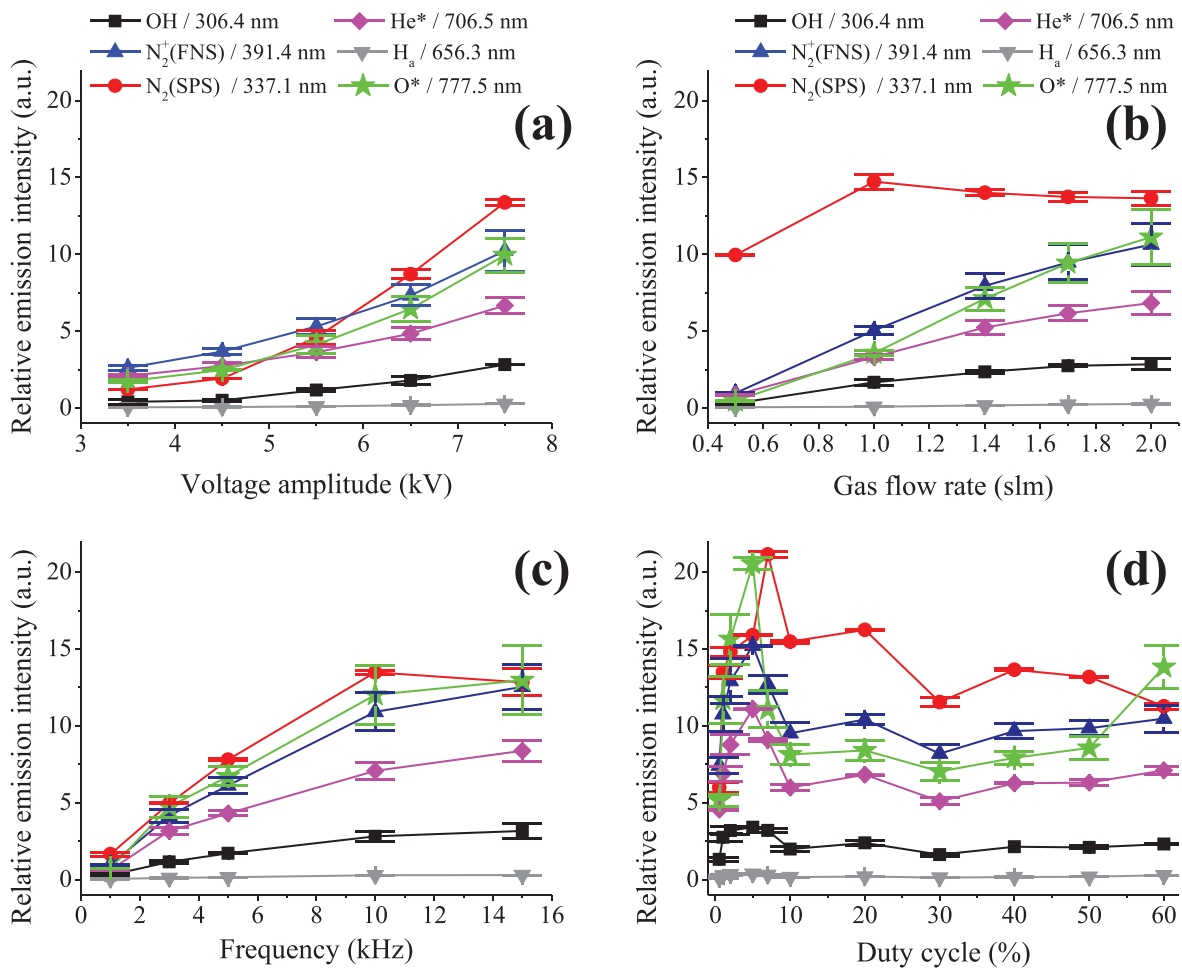


FIG. 6. Relative emission intensity of main excited species (see the insets) vs (a) voltage amplitude, (b) helium flow rate, (c) voltage frequency, and (d) voltage duty cycle.

On the other hand, it has been proven that the drift of the residual charge under the influence of the local electric field is the main reason for the momentum and energy transfer to the surrounding neutrals and, eventually, for the development of the helium-air hydrodynamic field where both ionization fronts propagate.<sup>11,17</sup> It is also reminded that the noble gas highly facilitates the ionization processes because of the higher direct ionization coefficient compared to that of the atmospheric air, under the same reduced electric field.<sup>38</sup> Thus, a gas flow field rich in helium (e.g., a laminar channel where weak helium-air mixing takes place) helps the front propagation. Consequently, the ionic species, which provoke the above electrohydrodynamic forces, depend on the gas channel composition and, vice versa, the resultant hydrodynamic profile determines the helium-air mixing and, thus, the kinetics in the channel. A complicated interplay, thus, takes place.

Based on this concept, the present results obtained for different voltage amplitudes and gas flow rates can readily be explained qualitatively. A higher gas flow rate increases the helium molar fraction in air, and a longer channel of high direct ionization coefficient is formed.

As far as the gas flow field is laminar, the higher voltage enhances the electric field and the subsequent ionization. Therefore, it is not surprising that longer plasma jet [Figs. 3(a) and 3(b)], faster ionization fronts [Figs. 4(a) and 4(b)], and enhanced chemical reactivity [Figs. 6(a), 6(b), 7(a), 7(b), 8(a), and 8(b)] are observed.

The present results demonstrate two interesting effects, i.e., the intense turbulent structure of the plasma jet for a frequency around 3 kHz [Fig. 3(c)] and the optimal chemical reactivity obtained for a duty cycle value around 5%–7% [Figs. 6(d), 7(d), 8(d)].

Frequency-dependent exotic plasma jet structures have been previously reported for different setups and working conditions (e.g., Refs. 39 and 40) although an overall interpretation has not yet been stated. Electrohydrodynamic effects, affected by the frequency and the duty cycle through the residual charge model,<sup>11,17</sup> should certainly be considered for this interpretation, but a complementary approach is presented here. From a fluid-mechanics point of view, it has been shown that the length of the laminar region of a free jet of neutrals depends—besides the Reynolds number—on the velocity profile at the nozzle's exit and on the growth rate of perturbations along the jet.<sup>41</sup>



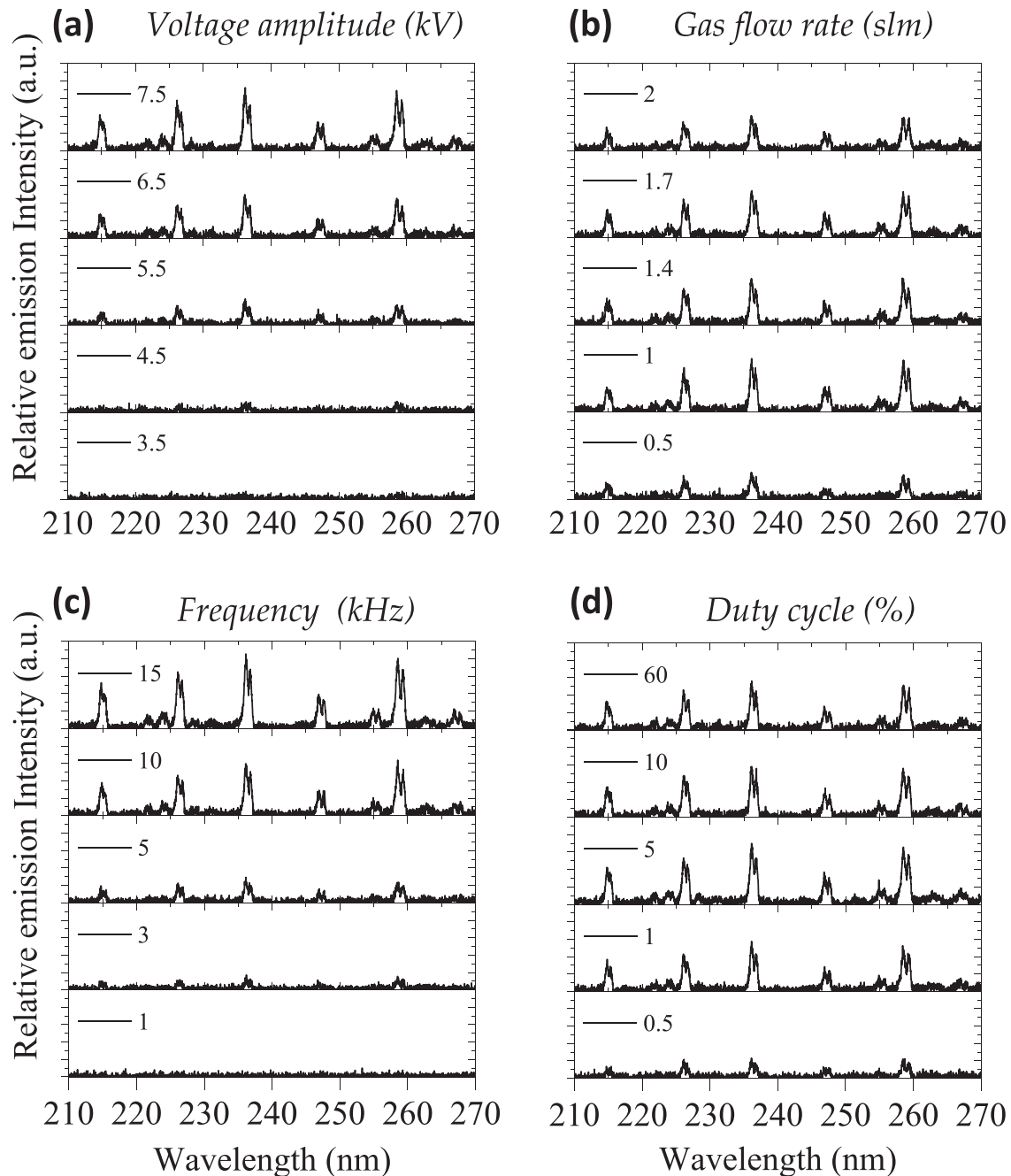


FIG. 7. Representative NO<sub>7</sub> spectra (UV-C) vs: (a) voltage amplitude, (b) helium flow rate, (c) voltage frequency, and (d) voltage duty cycle.

Using varicose perturbations, i.e., mechanical perturbations induced by a loudspeaker, Crow and Champagne<sup>42</sup> found that the flow response is a function of the forcing frequency and that for air jets, the maximum amplification occurs at a Strouhal number of 0.3. This result has been confirmed in numerous studies for a wide range of operating conditions.<sup>43</sup> At forcing frequencies that correspond to this

“preferred mode,” the vortical structures that are responsible for the breakdown of the laminar jet are intensified, leading to a shorter laminar region.<sup>44</sup> Although these results concern air jets propagating in ambient air, a similar behavior of variable density jets can be assumed. This means that there is a specific forcing frequency of helium that perturbs the gas flow field and shortens the laminar flow. Shorter

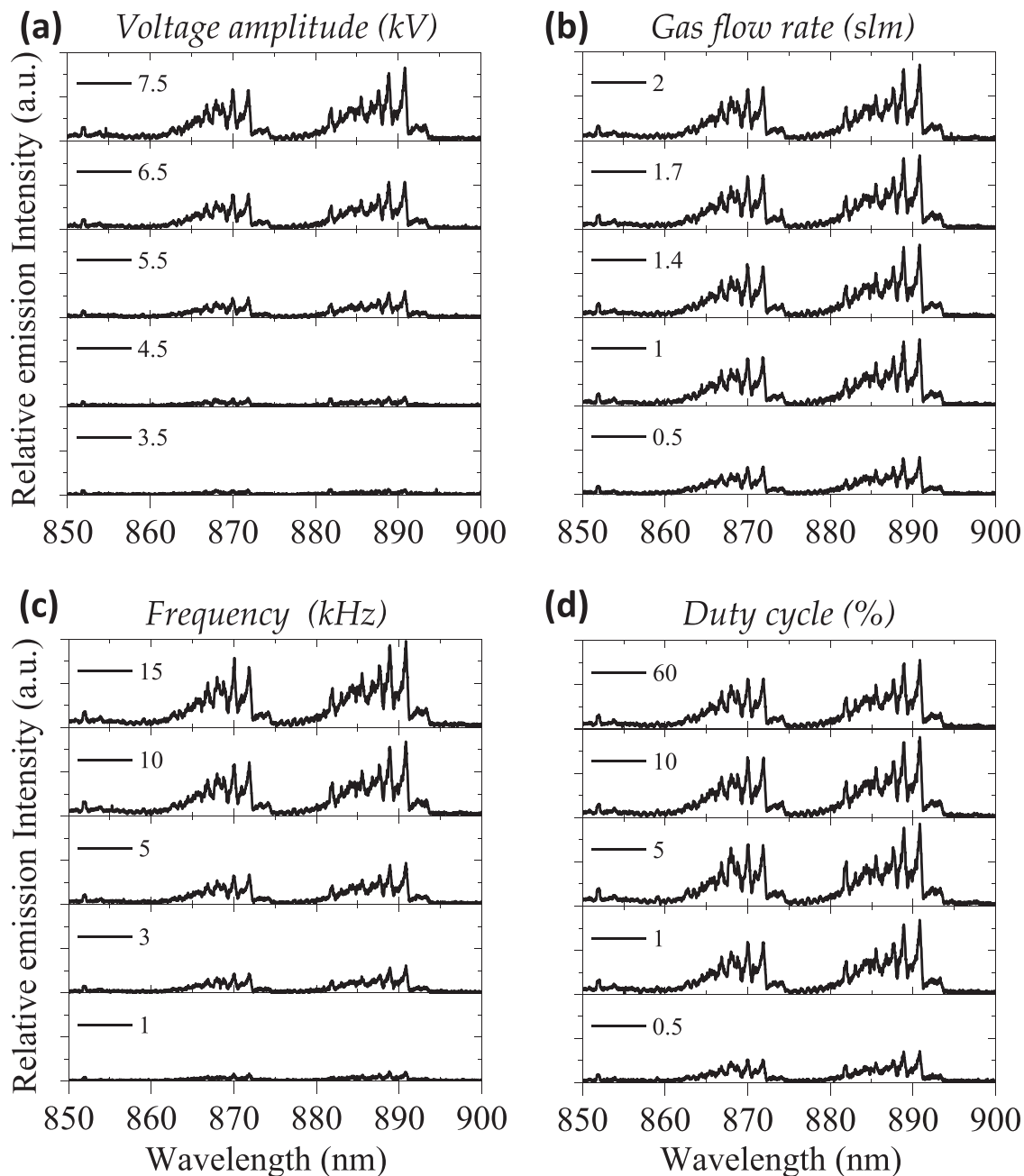
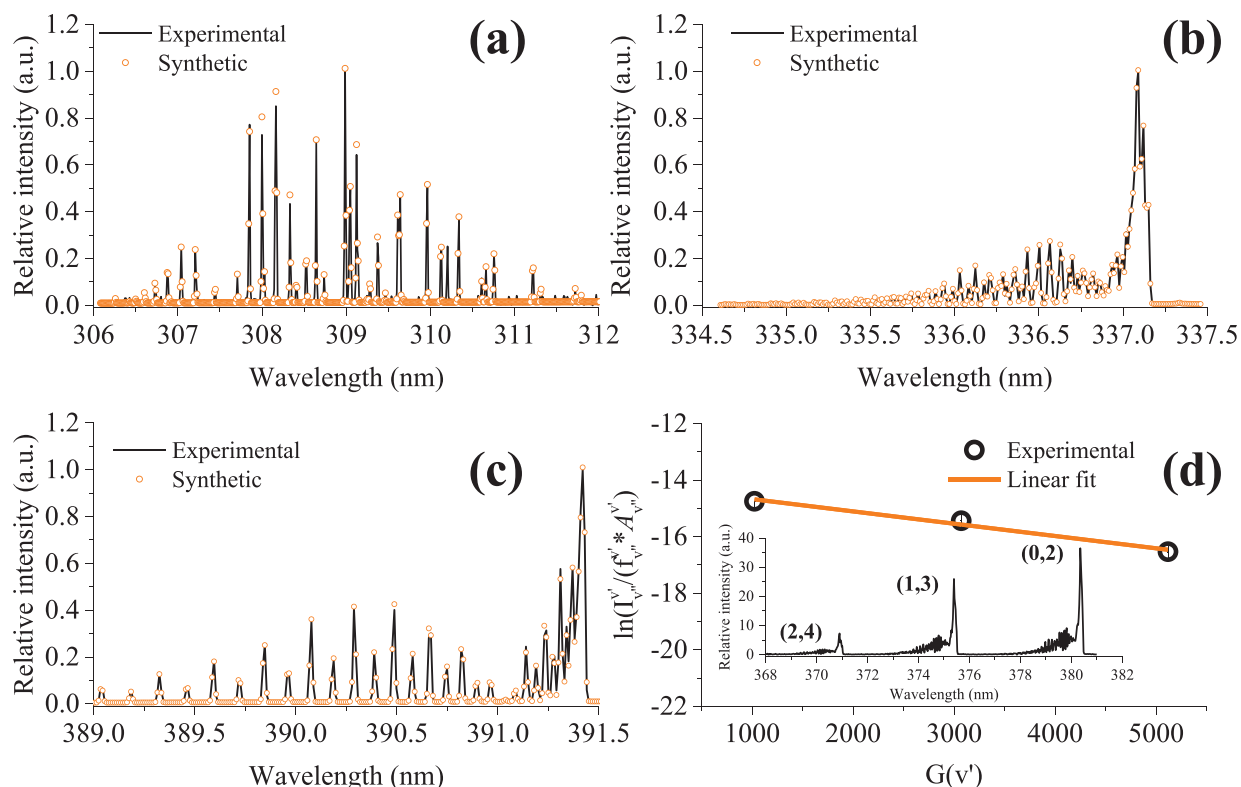


FIG. 8. Representative  $N_2(FPS)$  spectra (IR-A) vs: (a) voltage amplitude, (b) helium flow rate, (c) voltage frequency, and (d) voltage duty cycle.

laminar flow means higher helium-air mixing and, thus, a lower direct ionization coefficient. Kyle and Sreenivasan<sup>45</sup> examined the instability of a helium jet propagating in ambient air and found that shear layer disturbances occur in a frequency range around 4 kHz, depending on the velocity. In the plasma jet case, this forcing frequency, corresponding to the preferred mode, is imposed by the driving high voltage and it is found here to be close to 3 kHz.

Regarding the reactive species production, there is an optimum duty cycle of around 5%–7% [ $5\text{--}7\ \mu\text{s}$  in Figs. 6(d), 7(d), 8(d)]. This result is in perfect agreement with the relative yield of radicals and positive and negative ions found by Liu *et al.*<sup>46</sup> In their report, a coaxial electrode configuration driven by square high voltage pulses is also used, but the inner electrode is covered by quartz. Thus, the above optimal was mainly ascribed to the accumulation of space charges that



**FIG. 9.** Representative high-resolution rotational distributions of different probe molecules: (a) OH(A-X), (b) N<sub>2</sub>(SPS), and (c) N<sub>2</sub><sup>+</sup>(FNS). The experimental rotational structures (in black) are fitted with the corresponding synthetic ones (in orange) for the estimation of the rotational temperature of the excited states. (d) Representative Boltzmann plot and vibrational spectrum of the N<sub>2</sub>(SPS) (inset, vibrational sequence  $\Delta v = -2$ ) used for the estimation of the vibrational temperature.

lead to the weakening of the reduced electric field with an increase in the pulse width beyond 10  $\mu$ s.<sup>46</sup> But, as it was mentioned above, this should not be the case for the present setup. Ono *et al.*<sup>47</sup> reported that a short-pulse air streamer is desirable for the high efficiency production of radicals and excited species, such as OH, O, or O<sub>3</sub>. Hoder *et al.*<sup>48</sup> reported that the discharge ignition on the falling slope of the high voltage pulse strongly relies on the pulse width in nitrogen-oxygen mixture barrier discharges at atmospheric pressure. With the duty-off cycle varying from 0.1 ms to 1 s, Wu *et al.*<sup>49</sup> found that the repeatability of the plasma bullet propagation in atmospheric-pressure plasma jets is strongly affected by the residual charge density. Lu *et al.*<sup>50</sup> measured the electric field in both the primary discharge (positive slope of the pulse) and the secondary discharge (negative slope of the pulse) by noninvasive Stark polarization spectroscopy. They found that the plasma plume length decreases vs the duty cycle, whereas the electric field corresponding to the primary discharge remains almost unaffected. The secondary discharge yields an electric field lower than 6 kV cm<sup>-1</sup>, i.e., much lower than that found in the primary one (9–17 kV cm<sup>-1</sup>).<sup>50</sup> These data support the above-mentioned concept that the second ionization front is subjected to a weaker electric field and a longer pulse width affects mainly this front. The second ionization front contributes to the plasma jet properties even though it is weaker compared to the first front.

Finally, it has been shown that for an electrode configuration like the one employed here, the electrical power is mainly dissipated as heat in the interface formed by the dielectric barrier and the operating gas and in the dielectric barrier itself. The gas along the plasma jet is mainly heated due to heat convection from the dielectric. Compared to the device in Ref. 22, the heating is less because the quartz tube leads to lower heating than an alumina tube does. Furthermore, a longer grounded external electrode provokes higher power consumption and higher temperatures.<sup>22</sup> Here, due to the short, grounded electrode (Fig. 1) and the low DBD mean power (about 150 mW at the default working conditions), the gas temperature remains low (Fig. 10).

## V. CONCLUSIONS

A helium plasma jet was produced by a coaxial DBD-based electrode configuration driven by high voltage square pulses and probed through the UV-to-NIR emission. Two discrete ionization fronts were generated by different discharge regimes. The first was due to the positive edge of the pulse and was related to a cathode-directed streamer propagating into the helium channel. The second front was due to the negative edge of the pulse and was related to the residual ionic space charge formed in the wake of the cathode-directed streamer propagation. It was found that the plasma properties are principally determined by the first front associated with a high local electric field, but they are also affected by the intensity of the second front, which is

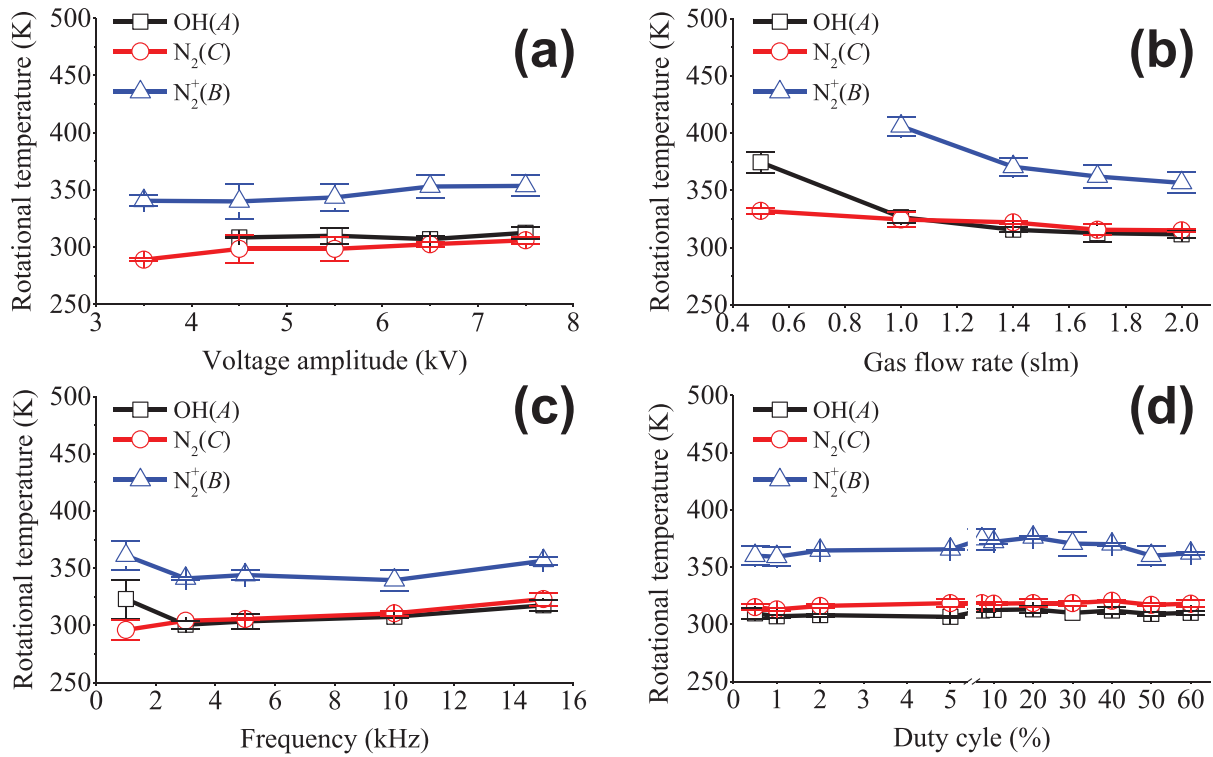


FIG. 10. Rotational temperature of three probe-excited species (see the insets) vs (a) voltage amplitude, (b) helium flow rate, (c) voltage frequency, and (d) voltage duty cycle.

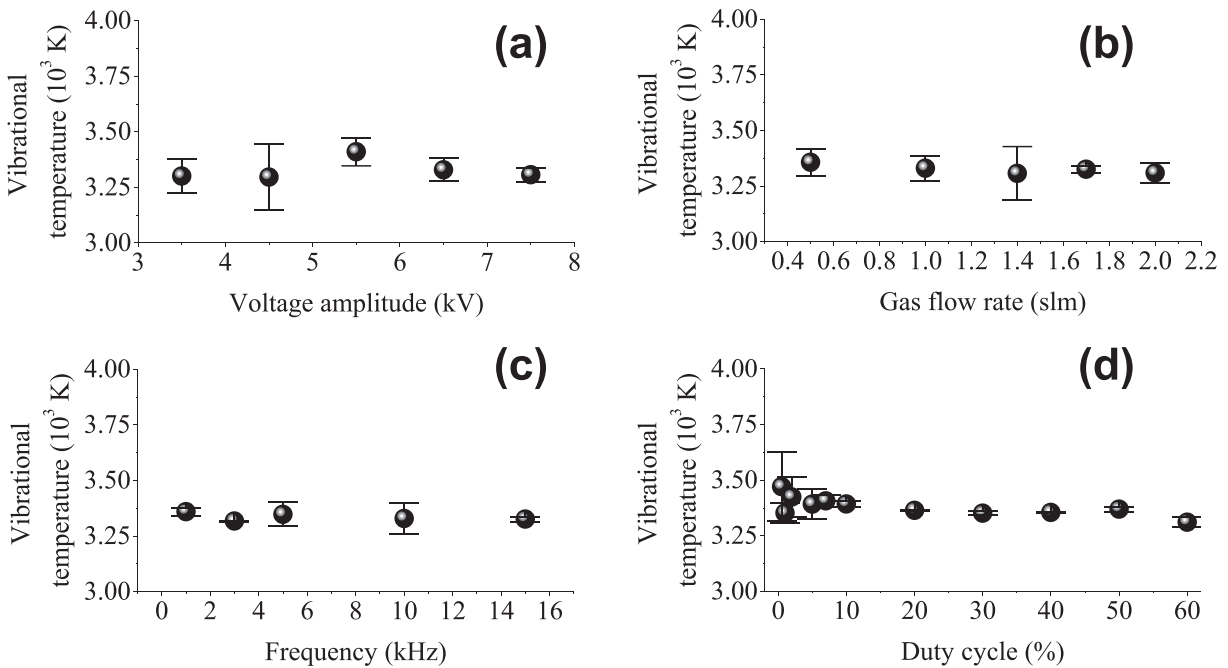


FIG. 11. N<sub>2</sub>(SPS) ( $\Delta v = -2$ ) vibrational temperature vs (a) voltage amplitude, (b) helium flow rate, (c) voltage frequency, and (d) voltage duty cycle.

associated with a lower local electric field. The voltage amplitude variation up to 7.5 kV led to the plasma jet length increase up to about 50 mm, the first front mean velocity increase to about  $3.5 \times 10^7 \text{ cm s}^{-1}$ , and the second front mean velocity increase to about  $2 \times 10^7 \text{ cm s}^{-1}$ . Increasing the voltage led to the increase in the relative density of the reactive species, whereas the gas temperature remained almost constant around 300–325 K. The gas flow rate variation up to 2 slm led to the plasma jet length increase up to about 50 mm, the first front mean velocity increase up to about  $3.5 \times 10^7 \text{ cm s}^{-1}$ , the second front mean velocity increase up to about  $2 \times 10^7 \text{ cm s}^{-1}$ , the increase in the emission intensity of copious reactive species, and a slight cooling of the gas. The voltage frequency variation up to 15 kHz led to the plasma jet length increase up to about 50 mm; the practically constant mean velocity of the first front, i.e.,  $3\text{--}3.5 \times 10^7 \text{ cm s}^{-1}$ ; the second front mean velocity continuous increase up to about  $2.5 \times 10^7 \text{ cm s}^{-1}$ ; the increase in the emission intensity of copious reactive species; and an almost constant gas temperature of about 300–325 K. The frequency of 3 kHz gave an unexpected turbulent structure of the plasma jet, which was attributed to the breakdown of the helium laminar region due to electro-hydrodynamic forces exerted by the ionic residual charge. The voltage duty cycle variation up to 60% led to: the plasma jet length decrease down to about 35 mm; a slight decrease in the mean velocity of the first front, i.e., a reduction of about  $0.5 \times 10^7 \text{ cm s}^{-1}$ ; an important decrease in the mean velocity of the second front, i.e., a reduction of about  $2.5 \times 10^7 \text{ cm s}^{-1}$ ; and an almost constant gas temperature of 300–325 K. An optimum duty cycle between 5% and 7% yielded the highest production of emissive reactive species. The distinct role of the duty cycle in the plasma features was emphasized and related to the local electric field and the space charge density during the propagation of the second ionization front.

## ACKNOWLEDGMENTS

This work was financially supported by the French ANR program PLASMINF (Grant No. UB: 904-CR: 200\_ECA-S/CR: X\_200\_PLASMINF). Kristaq Gazeli also acknowledges funding from European Union's Horizon 2020 research and innovation program under Grant Agreement No. 810686 for visiting University of Cyprus in the frame of this work.

## DATA AVAILABILITY

The data that support the findings of this study are available from the corresponding author upon reasonable request.

## REFERENCES

- I. C. Gerber, I. Mihaila, V. Pohoata, and I. Topala, "Evolution of electrical and optical parameters of a helium plasma jet in interaction with liquids," *IEEE Trans. Plasma Sci.* (published online 2020).
- G. B. Sretenović, I. B. Krstić, V. V. Kovačević, B. M. Obradović, and M. M. Kuraica, "Spatio-temporally resolved electric field measurements in helium plasma jet," *J. Phys. D: Appl. Phys.* **47**, 102001 (2014).
- A. Stancampiano, E. Simoncelli, M. Boselli, V. Colombo, and M. Gherardi, "Experimental investigation on the interaction of a nanopulsed plasma jet with a liquid target," *Plasma Sources Sci. Technol.* **27**, 125002 (2018).
- K. Gazeli, T. Vazquez, G. Bauville, N. Blin-Simiand, B. Bournonville, S. Pasquiers, and J. S. Sousa, "Experimental investigation of a ns-pulsed argon plasma jet for the fast desorption of weakly volatile organic compounds deposited on glass substrates at variable electric potential," *J. Phys. D: Appl. Phys.* **53**, 475202 (2020).
- T.-H. Chung, A. Stancampiano, K. Sklias, K. Gazeli, F. M. André, S. Dozias, C. Douat, J.-M. Pouvesle, J. S. Sousa, E. Robert, and L. M. Mir, "Cell electroporation enhancement by non-thermal-plasma-treated PBS," *Cancers* **12**, 219 (2020).
- F. Vaquero, F. Judée, M. Vallette, H. Decauchy, A. Arbelaz, L. Aoudjehane, O. Scatton, E. Gonzalez-Sanchez, F. Merabtene, J. Augustin, C. Housset, T. Dufour, and L. Fouassier, "Cold-atmospheric plasma induces tumor cell death in preclinical in vivo and in vitro models of human cholangiocarcinoma," *Cancers* **12**, 1280 (2020).
- K. Gazeli, P. Svarnas, P. Vafeas, P. K. Papadopoulos, A. Gkelios, and F. Clément, "Investigation on streamers propagating into a helium jet in air at atmospheric pressure: Electrical and optical emission analysis," *J. Appl. Phys.* **114**, 103304 (2013).
- P. Svarnas, K. Gazeli, A. Gkelios, L. Amanatides, and D. Mataras, "On the reliable probing of discrete 'plasma bullet' propagation," *Meas. Sci. Technol.* **29**, 045016 (2018).
- F. Liu, L. Nie, X. Lu, J. Stephens, and K. Ostrikov, "Atmospheric plasma VUV photon emission," *Plasma Sources Sci. Technol.* **29**, 065001 (2020).
- J. Golda, B. Biskup, V. Layes, T. Winzer, and J. Benedikt, "Vacuum ultraviolet spectroscopy of cold atmospheric pressure plasma jets," *Plasma Processes Polym.* **17**, 1900216 (2020).
- P. Papadopoulos, D. Athanasopoulos, K. Sklias, P. Svarnas, N. Mourousias, K. Vratsinis, and P. Vafeas, "Generic residual charge based model for the interpretation of the electro-hydrodynamic effect in cold atmospheric pressure plasmas," *Plasma Sources Sci. Technol.* **28**, 065005 (2019).
- P. K. Papadopoulos, P. Vafeas, P. Svarnas, K. Gazeli, P. M. Hatzikonstantinou, A. Gkelios, and F. Clément, "Interpretation of the gas flow field modification induced by guided streamer ('plasma bullet') propagation," *J. Phys. D: Appl. Phys.* **47**, 425203 (2014).
- D. K. Logothetis, P. K. Papadopoulos, P. Svarnas, and P. Vafeas, "Numerical simulation of the interaction between helium jet flow and an atmospheric-pressure 'plasma jet,'" *Comput. Fluids* **140**, 11–18 (2016).
- R. Ohyama, M. Sakamoto, and A. Nagai, "Axial plasma density propagation of barrier discharge non-thermal plasma bullets in an atmospheric pressure argon gas stream," *J. Phys. D: Appl. Phys.* **42**, 105203 (2009).
- N. Ekem, T. Akan, Y. Akgun, A. Kiremitci, S. Pat, and G. Musa, "Sterilization of staphylococcus aureus by atmospheric pressure pulsed plasma," *Surf. Coat. Technol.* **201**, 993–997 (2006).
- J. Raiser and M. Zenker, "Argon plasma coagulation for open surgical and endoscopic applications: State of the art," *J. Phys. D: Appl. Phys.* **39**, 3520–3523 (2006).
- S. Park, U. Cvelbar, W. Choe, and S. Y. Moon, "The creation of electric wind due to the electrohydrodynamic force," *Nat. Commun.* **9**, 371 (2018).
- Q. Xiong, X. Lu, Y. Xian, J. Liu, C. Zou, Z. Xiong, W. Gong, K. Chen, X. Pei, F. Zou, J. Hu, Z. Jiang, and Y. Pan, "Experimental investigations on the propagation of the plasma jet in the open air," *J. Appl. Phys.* **107**, 073302 (2010).
- M. Laroussi, X. Lu, V. Kolobov, and R. Arslanbekov, "Power consideration in the pulsed dielectric barrier discharge at atmospheric pressure," *J. Appl. Phys.* **96**, 3028–3030 (2004).
- J. L. Walsh, P. Olszewski, and J. W. Bradley, "The manipulation of atmospheric pressure dielectric barrier plasma jets," *Plasma Sources Sci. Technol.* **21**, 034007 (2012).
- C. Monge-Daugé, F. Clément, P. Svarnas, J.-F. Loiseau, A. Ricard, and B. Held, "Experimental study coupled with electrical modelling for the consideration of DBD-based plasma jet," *IEEE Trans. Plasma Sci.* **40**, 2254–2260 (2012).
- P. Svarnas, P. Papadopoulos, D. Athanasopoulos, K. Sklias, K. Gazeli, and P. Vafeas, "Parametric study of thermal effects in a capillary dielectric-barrier discharge related to plasma jet production: Experiments and numerical modeling," *J. Appl. Phys.* **124**, 064902 (2018).
- R. P. Cardoso, T. Belmonte, P. Keravec, F. Kosior, and G. Henrion, "Influence of impurities on the temperature of an atmospheric helium plasma in micro-wave resonant cavity," *J. Phys. D: Appl. Phys.* **40**, 1394 (2007).
- K. Gazeli, C. Noël, F. Clément, C. Dauge, P. Svarnas, and T. Belmonte, "A study of helium atmospheric-pressure guided streamers for potential biological applications," *Plasma Sources Sci. Technol.* **22**, 025020 (2013).



- <sup>25</sup>P. J. Bruggeman, N. Sadeghi, D. C. Schram, and V. Linss, "Gas temperature determination from rotational lines in non-equilibrium plasmas: A review," *Plasma Sources Sci. Technol.* **23**, 023001 (2014).
- <sup>26</sup>T. Belmonte, C. Noël, T. Gries, J. Martin, and G. Henrion, "Theoretical background of optical emission spectroscopy for analysis of atmospheric pressure plasmas," *Plasma Sources Sci. Technol.* **24**, 064003 (2015).
- <sup>27</sup>I. Sremački, M. Gromov, C. Leys, R. Morent, R. Snyders, and A. Nikiforov, "An atmospheric pressure non-self-sustained glow discharge in between metal/metal and metal/liquid electrodes," *Plasma Processes Polym.* **17**, 1900191 (2020).
- <sup>28</sup>A. Fridman and L. A. Kennedy, *Plasma Physics and Engineering* (Taylor and Francis Group, New York, 2004).
- <sup>29</sup>N. Masoud, K. Martus, M. Figus, and K. Becker, "Rotational and vibrational temperature measurements in a high-pressure cylindrical dielectric barrier discharge (C-DBD)," *Contrib. Plasma Phys.* **45**, 32–39 (2005).
- <sup>30</sup>P. Svarnas, "Vibrational temperature of excited nitrogen molecules detected in a 13.56 MHz electrical discharge by sheath-side optical emission spectroscopy," *Plasma Sci. Technol.* **15**, 891–895 (2013).
- <sup>31</sup>K. Gazeli, P. Svarnas, B. Held, L. Marlin, and F. Clément, "Possibility of controlling the chemical pattern of He and Ar 'guided streamers' by means of N<sub>2</sub> or O<sub>2</sub> additives," *J. Appl. Phys.* **117**, 093302 (2015).
- <sup>32</sup>X. Lu, M. Laroussi, and V. Puech, "On atmospheric-pressure non-equilibrium plasma jets and plasma bullets," *Plasma Sources Sci. Technol.* **21**, 034005 (2012).
- <sup>33</sup>F. Girard, V. Badets, S. Blanc, K. Gazeli, L. Marlin, L. Authier, P. Svarnas, N. Sojic, F. Clément, and S. Arbault, "Formation of reactive nitrogen species including peroxyinitrite in physiological buffer exposed to cold atmospheric plasma," *RSC Adv.* **6**, 78457–78467 (2016).
- <sup>34</sup>F. Girard, M. Peret, N. Dumont, V. Badets, S. Blanc, K. Gazeli, C. Noël, T. Belmonte, L. Marlin, J.-P. Cambus, G. Simon, N. Sojic, B. Held, S. Arbault, and F. Clément, "Correlations between gaseous and liquid phase chemistries induced by cold atmospheric plasmas in a physiological buffer," *Phys. Chem. Chem. Phys.* **20**, 9198 (2018).
- <sup>35</sup>K. Gazeli, G. Bauville, M. Fleury, P. Jeanney, O. Neveu, S. Pasquiers, and J. S. Sousa, "Effect of the gas flow rate on the spatiotemporal distribution of Ar(1s<sub>5</sub>) absolute densities in a ns pulsed plasma jet impinging on a glass surface," *Plasma Sources Sci. Technol.* **27**, 065003 (2018).
- <sup>36</sup>Q. Xiong, A. Y. Nikiforov, X. P. Lu, and C. Leys, "High-speed dispersed photographing of an open-air argon plasma plume by a grating-ICCD camera system," *J. Phys. D: Appl. Phys.* **43**, 415201 (2010).
- <sup>37</sup>H. S. Park, S. J. Kim, H. M. Joh, T. H. Chung, S. H. Bae, and S. H. Leem, "Optical and electrical characterization of an atmospheric pressure microplasma jet with a capillary electrode," *Phys. Plasmas* **17**, 033502 (2010).
- <sup>38</sup>J.-P. Boeuf, L. L. Yang, and L. C. Pitchford, "Dynamics of a guided streamer ('plasma bullet') in a helium jet in air at atmospheric pressure," *J. Phys. D: Appl. Phys.* **46**, 015201 (2013).
- <sup>39</sup>T. Darny, E. Robert, D. Riès, S. Dozias, and J. Pouvesle, "Unexpected plasma plume shapes produced by a microsecond plasma gun discharge," *IEEE Trans. Plasma Sci.* **42**, 2504–2505 (2014).
- <sup>40</sup>Y. B. Xian, M. H. Qaisrani, Y. F. Yue, and X. P. Lu, "Discharge effects on gas flow dynamics in a plasma jet," *Phys. Plasmas* **23**, 103509 (2016).
- <sup>41</sup>J. Zayko, S. Teplovodskii, A. Chicherina, V. Vedeneev, and A. Reshmin, "Formation of free round jets with long laminar regions at large Reynolds numbers," *Phys. Fluids* **30**, 043603 (2018).
- <sup>42</sup>S. C. Crow and F. H. Champagne, "Orderly structure in jet turbulence," *J. Fluid Mech.* **48**, 547–591 (1971).
- <sup>43</sup>X. Garnaud, L. Lesshafft, P. J. Schmid, and P. Huerre, "Modal and transient dynamics of jet flows," *Phys. Fluids* **25**, 044103 (2013).
- <sup>44</sup>T. B. Gohil, A. K. Saha, and K. Muralidhar, "Direct numerical simulation of forced circular jets: Effect of varicose perturbation," *Int. J. Heat Fluid Flow* **44**, 524–541 (2013).
- <sup>45</sup>D. M. Kyle and K. R. Sreenivasan, "The instability and breakdown of a round variable-density jet," *J. Fluids* **249**, 619–664 (1993).
- <sup>46</sup>Z. Liu, C. Zhou, D. Liu, D. Xu, W. Xia, Q. Cui, B. Wang, and M. G. Kong, "Production and correlation of reactive oxygen and nitrogen species in gas- and liquid-phase generated by helium plasma jets under different pulse widths," *Phys. Plasmas* **25**, 013528 (2018).
- <sup>47</sup>R. Ono, Y. Nakagawa, and T. Oda, "Effect of pulse width on the production of radicals and excited species in a pulsed positive corona discharge," *J. Phys. D: Appl. Phys.* **44**, 485201 (2011).
- <sup>48</sup>T. Hoder, H. Hoefl, M. Kettlitz, K. Weltmann, and R. Brandenburg, "Barrier discharges driven by sub-microsecond pulses at atmospheric pressure: Breakdown manipulation by pulse width," *Phys. Plasmas* **19**, 070701 (2012).
- <sup>49</sup>S. Wu, X. Lu, D. Liu, Y. Yang, Y. Pan, and K. Ostrikov, "Photo-ionization and residual electron effects in guided streamers," *Phys. Plasmas* **21**, 103508 (2014).
- <sup>50</sup>Y. Lu, S. Wu, W. Cheng, and X. Lu, "Electric field measurements in an atmospheric-pressure microplasma jet using Stark polarization emission spectroscopy of helium atom," *Eur. Phys. J. Spec. Top.* **226**, 2979–2989 (2017).
- <sup>51</sup>He metastables are efficiently produced with the present plasma jet as it is suggested from the higher rotational temperature of N<sub>2</sub><sup>+</sup>(B) compared to that of OH(A) and N<sub>2</sub>(C) (Fig. 10). Penning ionization is expected to be an efficient mechanism under the present experimental conditions leading to the ionization of N<sub>2</sub>(X) to the N<sub>2</sub><sup>+</sup>(B) state. Besides, the results of Fig. 8 reveal the formation of N<sub>2</sub>(A) metastables due to the radiative relaxation of N<sub>2</sub>(B) to the N<sub>2</sub>(A) state [i.e., N<sub>2</sub>(FPS) transition].